APPLIED SCIENCES AND ENGINEERING

An ultrahigh-resolution soft x-ray microscope for quantitative analysis of chemically heterogeneous nanomaterials

David A. Shapiro[1]*, Sergey Babin[2], Richard S. Celestre[1], Weilun Chao[3], Raymond P. Conley[4], Peter Denes[1], Bjoern Enders[1,5,6], Pablo Enfedaque[7], Susan James[8], John M. Joseph[9], Harinarayan Krishnan[1,7], Stefano Marchesini[1,7], Krishna Muriki[8], Kasra Nowrouzi[1,10], Sharon R. Oh[3], Howard Padmore[1], Tony Warwick[1], Lee Yang[9], Valeriy V. Yashchuk[1], Young-Sang Yu[1], Jiangtao Zhao[1,11]

The analysis of chemical states and morphology in nanomaterials is central to many areas of science. We address this need with an ultrahigh-resolution scanning transmission soft x-ray microscope. Our instrument provides multiple analysis tools in a compact assembly and can achieve few-nanometer spatial resolution and high chemical sensitivity via x-ray ptychography and conventional scanning microscopy. A novel scanning mechanism, coupled to advanced x-ray detectors, a high-brightness x-ray source, and high-performance computing for analysis provide a revolutionary step forward in terms of imaging speed and resolution. We present x-ray microscopy with 8-nm full-period spatial resolution and use this capability in conjunction with operando sample environments and cryogenic imaging, which are now routinely available. Our multimodal approach will find wide use across many fields of science and facilitate correlative analysis of materials with other types of probes.

INTRODUCTION

Scanning transmission x-ray microscopy (STXM) is a key analytical tool enabled by high-brightness x-ray synchrotrons, which can provide a wide variety of contrast mechanisms for studying material properties (*1*–*4*). High-energy (hard) x-rays give access to atomic fluorescence for quantifying elemental composition and also crystal lattice structure and strain through Bragg diffraction. Meanwhile, lower-energy (soft) x-rays are sensitive to more complex chemistries, magnetic states, and bond orientation. Regardless of the contrast mechanism in use, the spatial resolution has, until recently, been limited by the nature of x-ray focusing optics, which, in general, image at resolutions many times the x-ray wavelength. This has limited the application of scanning x-ray microscopes to a certain extent but they still find very broad use in the materials, environmental, and life sciences.

The performance of scanning microscopes, as characterized by speed, sensitivity, and achievable resolution, is determined largely by the x-ray source brightness, numerical aperture (NA) and efficiency of the nanofocusing x-ray optics, instrument stability, detection efficiency, sample contrast, and its tolerance of radiation dose. Because of the difficulty in producing optics, which efficiently focuses x-rays to very small spots (sub–10 nm) with practical working distance, it is advantageous to develop imaging schemes that are not limited by the available NA. Conventional x-ray microscopy has developed into a high-throughput tool with around 30-nm spatial resolution. A 10-nm half-period resolution has been reported (*5*–*7*), in both full-field and scanning modes, but microscopy at such high resolution is particularly challenging at longer wavelengths (>1 nm) where focal lengths become impractically small. X-ray ptychography, on the other hand, has seen rapid development as a coherent x-ray scattering–based imaging scheme, which holds great promise for surpassing the challenges associated with the development of high-resolution x-ray optics (*8*–*13*). For the case of ptychography, the only limitation on achievable resolution beyond instrument precision is scattering from the sample, which is a function of x-ray source brightness (coherent flux), wavelength, detection efficiency, and sample contrast. Hence, optimized instruments can, in fact, operate as x-ray wavelength–limited microscopes given adequate x-ray sources and detectors. The development of ptychographic microscopy is particularly important, as the synchrotron community invests in upgraded accelerator lattices that will deliver unprecedented coherent x-ray photon flux (*14*). The revolutionary brightness that will be enabled by these new x-ray synchrotron sources argues strongly for the development of ptychographic microscopes that will reduce the problem of high-resolution x-ray microscopy to one of the detection and analysis of scattered x-rays.

Ptychographic microscopes are developed by researchers at most synchrotrons around the world, and they are applied to a variety of scientific problems (*15*–*17*). However, routine use is still challenging because of the high-speed diffraction data acquisition and analysis pipeline, which is needed for convenient operation. We present here a user-friendly, multimodal microscope at the Advanced Light Source, which can transparently switch between conventional and ptychographic microscopy. Our instrument leverages a dedicated high-brightness x-ray source with broad tunable energy and polarization control, a high-performance scanning instrument in an actively controlled environment, a fast–frame rate charge-coupled device (CCD) detector, fully integrated high-performance computing for

[1]Advanced Light Source, Lawrence Berkeley National Laboratory, Berkeley, CA 94720, USA. [2]aBeam Technologies Inc., Hayward, CA 94541, USA. [3]Center for X-ray Optics, Lawrence Berkeley National Laboratory, Berkeley, CA 94720, USA. [4]Advanced Photon Source, Argonne National Laboratory, Argonne, IL 60439, USA. [5]Department of Physics, University of California, Berkeley, Berkeley, CA 94720, USA. [6]National Energy Research Scientific Computing Center, Berkeley, CA 94720, USA. [7]Computational Research Division, Lawrence Berkeley National Laboratory, Berkeley, CA 94720, USA. [8]Information Technology Division, Lawrence Berkeley National Laboratory, Berkeley, CA 94720, USA. [9]Engineering Division, Lawrence Berkeley National Laboratory, Berkeley, CA 94720, USA. [10]Advanced Quantum Testbed, Lawrence Berkeley National Laboratory, Berkeley, CA 94720, USA. [11]University of Science and Technology of China, Hefei, Anhui 230026, China.
*Corresponding author. Email: dashapiro@lbl.gov

transparent ptychographic analysis, and a suite of sample environments, compatible with transmission electron microscopy (TEM), for operando and cryogenic microscopy. The key achievement presented here is the tight integration of several advanced technologies into a unified scientific tool that fundamentally advances the capabilities of x-ray microscopy.

In the following sections, we quantify the performance of our microscope and describe various scientific applications. We present the highest-resolution x-ray images ever recorded, at 8-nm full-period oscillation, both from known test structures and from real nanomaterials using multiple sample environments including cryogenic samples and a high-temperature gaseous environment. We address one of the fundamental problems of spectromicroscopy, the inability to accurately quantify chemical composition in heterogeneous materials when the size of the chemical phases approaches the width of the microscope point spread function (PSF). An observed mixing of chemical composition at the interface of two phases can result from the tails of an imaging system's PSF and is exacerbated for microscopes with partially obstructed pupil functions, as is often the case for x-ray microscopes. Spectral mixing can occur over length scales a few times the Rayleigh resolution of the optic and can lead to substantial distortion when the phases are asymmetric in size or optical density. In the extreme case of biphasic systems with chemical phases smaller than the width of the PSF, the measured chemical phase distribution appears uniform or mixed. Thus, data interpretation must proceed carefully within the context of correlated measurements. X-ray ptychographic microscopy can be considered a noise-robust means of deconvolving the x-ray probe at length scales considerably smaller than the PSF of the illumination. We demonstrate how ptychographic imaging can extract accurate spectra from chemical phases with size near the x-ray spot, while conventional x-ray imaging cannot.

RESULTS

Resolution analysis

In the absence of mechanical limitations, the greatest obstacle to achieve high–spatial resolution (below 10 nm) ptychographic microscopy at modern synchrotrons is the contrast of the sample. Material contrast against vacuum, i.e., scattering cross section, increases rapidly with wavelength, so achieving high resolution with lighter elements becomes feasible with soft x-rays (below 2-keV photon energy). High resolution has been quantitatively demonstrated previously but never without the use of heavy metals such as Au or Pt (*9*, *18*, *19*). Here, we present a quantitative analysis of achieved spatial resolution using both idealized test structures with heavy elements as well as real nanomaterials made of lighter transition metals. We quantify the achieved spatial resolution of our microscope by measuring both one-dimensional and two-dimensional objects of known structure and composition. First, we study a binary pseudorandom multilayer pattern made of alternating layers of WSi_2 and Si with a minimum layer width of 3 nm (*20*, *21*). We image the structure with 10-ms exposures of 1300-eV x-rays and 0.95-nm wavelength. The detector geometry, described in the Supplementary Materials, allows for recording x-ray scattering to a full period of 7.7 nm, but the data were padded to provide a half-period pixel size of 3 nm in the reconstructed image. The roughly 100-nm-thick structure scatters the x-rays exclusively in the direction orthogonal to the lines (horizontally), and because of the high contrast and large bandwidth of the pseudorandom structure, the scattered intensity extends to the edge of the measurable NA (fig. S9). The binary linear pattern scatters very strongly in only one direction, but it allows for quantitative analysis of the maximum achievable spatial resolution in that direction. We analyze the achieved spatial resolution using two methods, Fourier ring correlation (FRC), which is now standard in the diffractive imaging community, as well as through the power spectral density (PSD) of the recovered image. For each case, the quantity is calculated for a single horizontal image line and then averaged for all lines in reciprocal space. The FRC calculation is explained in detail in the Supplementary Materials. The quantity analyzed is the scattering contrast, $s(\vec{x}) = \sqrt{\delta(\vec{x})^2 + \beta(\vec{x})^2}$, where $\delta(\vec{x})$ and $\beta(\vec{x})$ are the reconstructed maps of the optical density and phase and is similarly linear with material thickness (*22*). Figure 1B shows that the FRC maintains a high value out to the full NA, which reaches a full-period spatial frequency of 0.17 nm^{-1}, corresponding to 6-nm oscillation periods. Meanwhile, the PSD drops several decades at a full-period spatial frequency corresponding to about 8-nm periods, which is the maximum spatial frequency measured. The pseudorandom pattern has a flat power spectrum out to a cutoff frequency beyond our measurement, so the roll-off of the reconstructed PSD is a good measure of achieved spatial resolution. We show in figs. S1 and S2 that the FRC can overestimate the achieved spatial resolution, which must be oversampled by at least a factor of 2 by the reconstructed pixel size for high-fidelity imaging.

We further analyze a two-dimensional structure made of 30-nm-diameter nanoparticles of Fe_3O_4 that scatters isotropically but still exhibits high contrast when imaged on the Fe L_3 edge at 710 eV and 1.75-nm wavelength. We image the object using the low-resolution mode, single short exposure, and high-resolution, double-exposure mode (described in the "Data Acquisition and Analysis" section) to compare the achieved resolution in both modes. In both cases, the short exposures are 5 ms and the long exposure is 50 ms. Figure 1C shows a split image of a collection of particles where the top half is measured using single exposure and the bottom half is measured using double exposure. Using single exposures, the particles are just visible, while with double exposure, they are well resolved. The Fourier correlation (FC) analysis (Fig. 1D) indicates that the achieved resolutions for single- and double-exposure modes are 18- and 7.6-nm full period, respectively. Here, a spatial resolution of 7.6 nm is just 4.3 times the wavelength of the x-ray illumination.

Spectromicroscopy

One of the key analytical capabilities of x-ray microscopy is the quantification of chemical states through imaging around molecular resonances (*23*, *24*). Soft x-rays, in particular, offer very high chemical contrast in the near-edge region and are sensitive to chemical bonding states in addition to atomic species. Scanning microscopy also offers the advantage, versus full-field imaging, of a uniform and constant illumination, which improves quantification but is necessarily slower because of the need for mechanical scanning. It also makes possible methods based on coherent scattering like ptychography. Quantitative spectromicroscopy requires imaging a material at several energies below, through, and above the relevant bond resonant energies. This provides an energy spectrum at each point in the sample, which can be normalized and fit with a linear combination of independently measured reference spectra for composition analysis. When reference spectra are not available, the measured

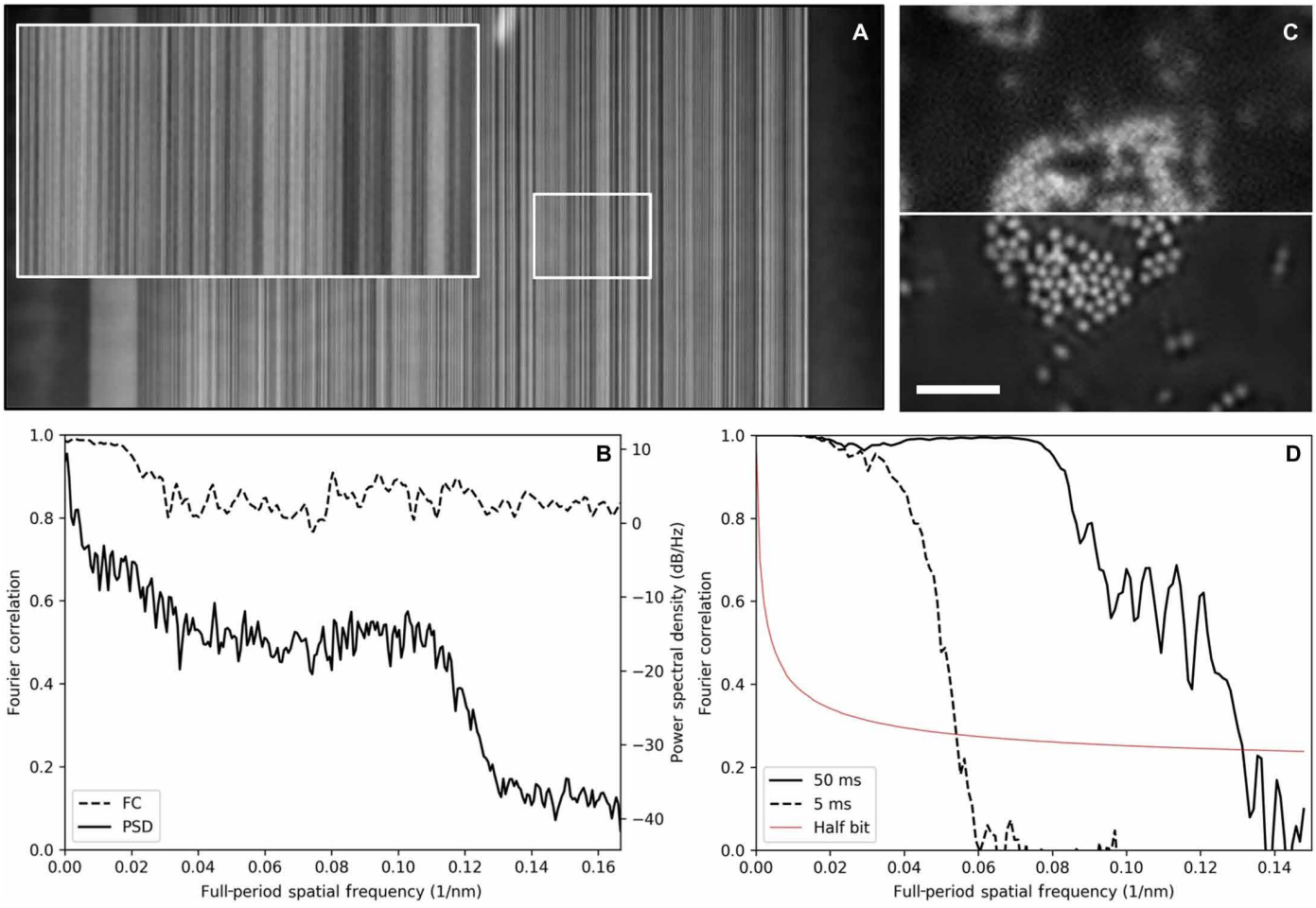

Fig. 1. Analysis of the microscope imaging resolution. (**A**) Ptychographic scattering contrast image of a linear test pattern with 3-nm smallest features. The inset image is 1 μm wide. (**B**) FC and PSD analysis of the reconstructed image, averaged by horizontal line. The FC shows high correlation to a full-period resolution of 6 nm (reconstructed pixel size of 3 nm), while the PSD shows a roll-off at 8-nm full-period resolution. (**C**) Ptychographic optical density of a collection of Fe_3O_4 nanoparticles. The top half image uses a 5-ms x-ray exposure time, while the bottom half uses 50-ms exposure. Scale bar, 1 μm; pixel size, 3 nm. (**D**) FC analysis of the two exposure times, which indicate full-period spatial resolutions of 18 and 7.6 nm for the 5- and 50-ms exposure times, respectively.

spectra can simply be interpreted for qualitative analysis. Here, we demonstrate chemical mapping in both conventional scanning and ptychographic modes and show how qualitative interpretation of the measured spectra can be improved by the high spatial resolution provided by ptychographic imaging.

As a model system, we image chemically delithiated particles of Li_xFePO_4 ($x \sim 0.5$), which is a battery cathode material in which the presence of lithium can be identified by the oxidation state of iron, which is reduced by the introduction of a lithium ion into the crystal unit cell. When partially delithiated, microplates of Li_xFePO_4 ($x \sim 0.5$) exhibit a core-shell structure where the shell is fully delithiated $FePO_4$ and the particle interior may contain a more mixed state with regions around morphological defects being more delithiated (*25*). Figure 2 shows results obtained in both imaging modes available in our microscope. Conventional STXM visualizes the large-scale structure and chemical features, whereas ptychographic mode can readily visualize the smallest nanoscale structures. The overall chemical maps are in qualitative agreement, but the ptychographic chemical map displays nanoscale chemical phases in the particle interior, which are not visible in conventional imaging mode. In this case, the chemical maps are obtained with a linear combination of reference spectra measured from nanoparticles of pure materials (*22*); thus, they represent quantitative composition with red being $FePO_4$ and green being $LiFePO_4$. The radiation dose delivered to the sample is estimated in fig. S8.

Figure 2E shows a comparison of extracted point spectra with the reference spectra where the points are chosen from the fully delithiated shell and the partially delithiated interior. The conventional spectrum from the shell region seems to show a more mixed content than should be present. This is apparent from the reduced peak height at 710 eV (highest absorption feature of $FePO_4$) relative to the peak at 708 eV (highest absorption feature of $LiFePO_4$). It is already known that the shell region should be pure $FePO_4$ except for a small percentage because of miscibility of the two phases (*26*). This is not apparent from the conventional spectra since the spectra of neighboring chemical phases tend to be mixed because of the finite spatial resolution. What is unexpected is the long length scale over which this spectral mixing occurs. The region in question here is several

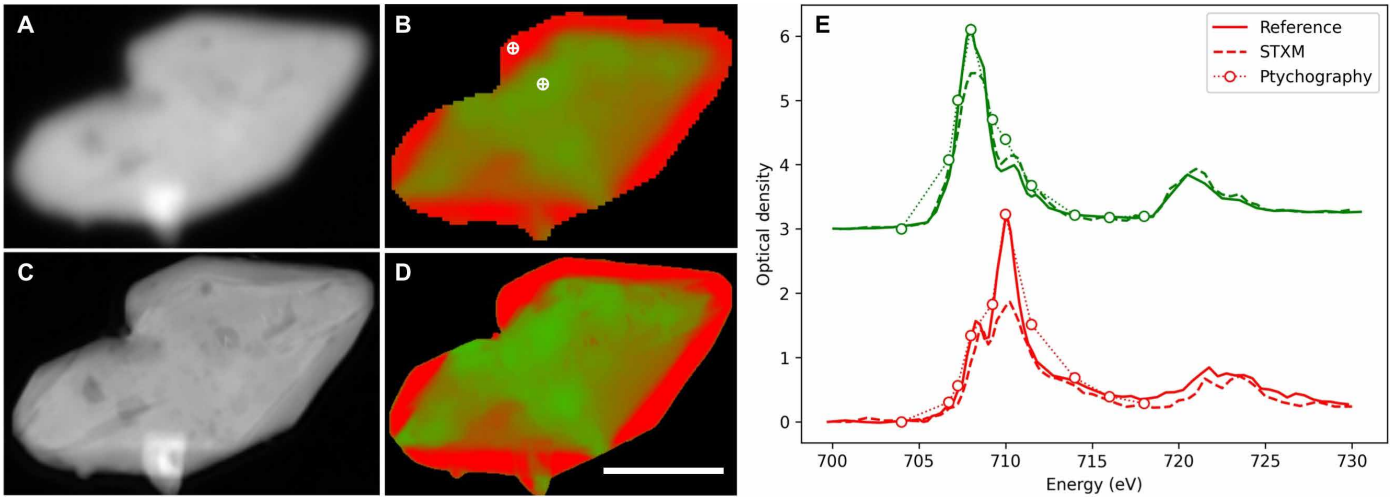

Fig. 2. Spectromicroscopy of a Li_xFePO_4 microplatelet. Conventional (**A** and **B**) and ptychographic (**C** and **D**) spectromicroscopy of Li_xFePO_4 microplatelets. Shown are the average optical density (A and C) and the chemical composition map (B and D) where the two chemical components ($LiFePO_4$ and $FePO_4$) are presented in green and red, respectively. Scale bar, 1 μm; reconstructed pixel size, 5 nm. Point spectra from conventional scanning (dashed lines) and ptychographic modes (dotted lines with circles) are shown in (**E**). Reference spectra from pure materials ($LiFePO_4$, green solid line; $FePO_4$, red solid line) are also shown for comparison. The conventional STXM spectra show distortions that favor the physically larger chemical phase, whereas the ptychographic spectra more closely match the references. The reference and STXM spectra use a 0.5-eV energy step from 706 to 712 eV and a 1-eV energy step otherwise.

times larger than the Rayleigh resolution of the focusing optic or about 150 nm compared to 55 nm. This indicates that the tails of the PSF contribute significantly to spectral features extracted from conventional data and that pure spectra can only be obtained from very large chemical phases, at least three times the Rayleigh resolution. The extracted ptychographic spectra, on the other hand, match closely the structure of the reference spectra, as we would expect for this particular material. This indicates that ptychographic imaging does effectively deconvolve the effect of the probe, thus providing purer spectra, and that conventional spectromicroscopy data must be carefully interpreted, usually within the context of correlative measurements.

Operando microscopy

A central design goal for our microscope is compatibility with commercial sample environments that will accelerate the implementation of operando imaging of active materials and will facilitate correlative measurements with electrons. To this end, we make available two sample holders designed by Hummingbird Scientific for TEM: one for fluid flow with biasing for electrochemical measurements or with liquid heating and one for gas flow with sample heating. We briefly demonstrate the use of sample heating by imaging a temperature-induced chemical transformation in collection of nanoparticles of Li_xFePO_4 (overall size of 100 nm by 80 nm by 20 nm and composition, $Li_{0.5}FePO_4$), which have been predicted to show a transition from a two-phase distribution to a solid solution phase at high temperatures (*27*). Figure 3 shows images of a collection of particles at room temperature (left) and at 300°C (right). Each chemical map is generated from three images (the pre-edge energy 705 eV and the two peak energies 708 and 710 eV) and were collected about 10 min after temperature change to reduce the effects of sample drift. Although the integrated state of charge of the ensemble is preserved, there is a tendency toward a more intermediate state of charge, i.e., green changing to reddish yellow. Although properly interpreting data of this sort requires many measurements, controls to identify radiation damage as well as theoretical analysis, it is now routine to execute these measurements at high spatial resolution and chemical sensitivity.

Cryogenic microscopy

Imaging at low temperatures is critical for the preservation of soft matter systems when exposed to high doses of ionizing radiation (*11*, *28*–*33*). This is particularly important when studying hydrated biological samples such as cells and tissues and is finding increased usage with engineered materials such as polymer blends, hybrid biomaterials, and even with battery materials. For this type of research, we provide access to a cryogenic sample stage from Gatan (Elsa), customized from their standard TEM model for a rotated geometry, which provides cryo-sample transfer capability and temperature control above 100 K. Figure 4 shows images of a frozen hydrated yeast cell, *Saccharomyces cerevisiae*, in both conventional and ptychographic imaging modes. The sample was drop-cast on a TEM grid, plunge-frozen in liquid nitrogen, preserving an ice layer thickness of about 5 μm, transferred to the microscope cold, and imaged with 520-eV x-rays while maintained at 100 K temperature. The conventional image is normalized to optical density, whereas the ptychographic image displays scattering contrast. For off-resonant imaging, the inclusion of the phase component in the scattering quantity markedly improves overall contrast, as is apparent from the right image of Fig. 4 and which is well known from hard x-ray ptychographic imaging. A complex internal structure is apparent, which calls for proper preparation by rapid freezing in liquid ethane and tomographic imaging for quantitative analysis (*11*, *28*–*33*). Using single-exposure-mode ptychography, with 10-ms exposures, the achieved spatial resolution is not substantially higher than conventional imaging mode.

DISCUSSION

The spatial resolution of an imaging system is defined as the minimum distance between two resolved structures and not the size of those structures, as is often implied. In a diffraction-based imaging

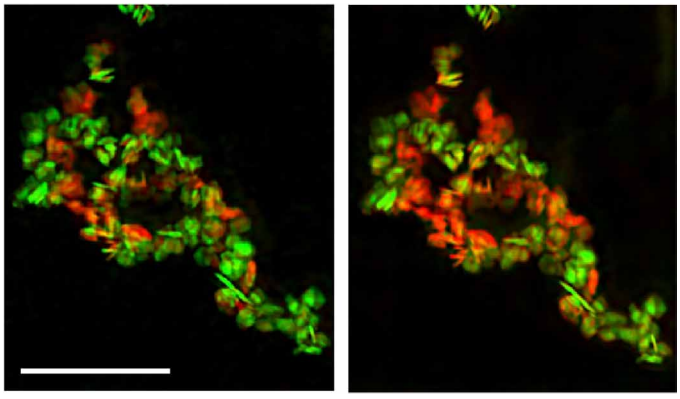

Fig. 3. Operando spectromicroscopy of a collection of Li_xFePO_4 nanoplatelets. The distribution of the chemical components, red ($FePO_4$) and green ($LiFePO_4$), is changed when the sample is heated to 300°C. Scale bar, 1 μm; pixel size, 5 nm.

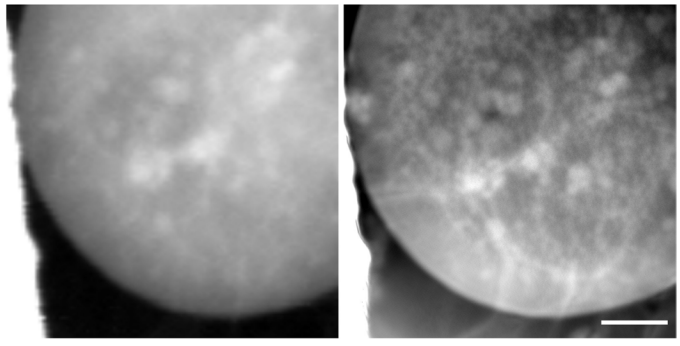

Fig. 4. Cryogenic microscopy of a frozen hydrated yeast cell. Conventional (**left**) and ptychographic (**right**) imaging of a frozen hydrated yeast cell using 520-eV x-rays. The ptychographic image shows scattering contrast and demonstrates improved contrast and resolution compared to conventional imaging. Scale bar, 1 μm; reconstructed pixel size, 5 nm.

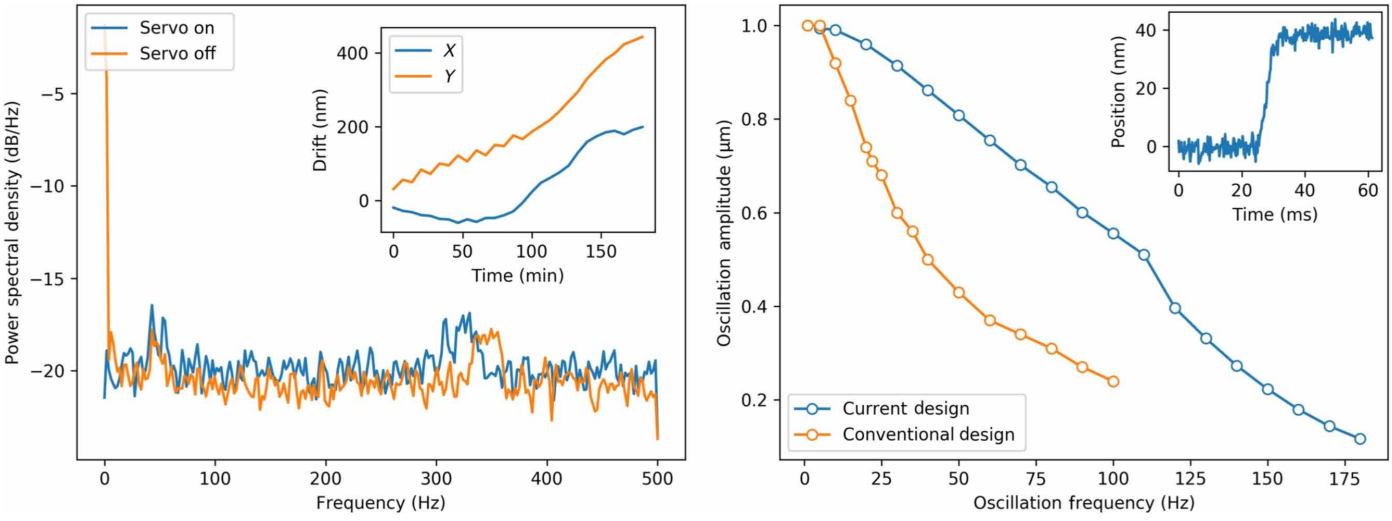

Fig. 5. Mechanical performance of the microscope. (**Left**) PSD of zone plate vibrations and sample drift (inset). The servo loop reduces mechanical drift but increases high-frequency vibrations slightly, while drift due to thermal effects is less than 2 nm/min. (**Right**) System bandwidth measurement of the new instrument and a conventional STXM design. The −1-dB oscillation amplitude is achieved at three times higher frequency, showing improved mechanical performance. The inset shows the step response for a 40-nm step, which is achieved in less than 10 ms.

system, the minimum period measured is λ/NA, which is given by the grating equation. For the case of ptychography, the detector geometry limits the NA and, hence, the sampling in the real space image with a pixel size, given by the Abbe equation, of λ/2NA. Faithful reproduction of structures in a discreet image requires more than two samples per full period, according to the Nyquist theorem. Although the achieved resolution in a ptychographic measurement depends on the statistics in the diffraction measurement (and other factors), the maximum achievable resolution is simply twice the pixel size, or 6 nm in our case, although the data are truncated at 7.7 nm because of padding beyond the detector width. We note that the FRC analysis consistently estimates the resolution to be finer than the maximum full period measured and that it has been proposed to use synthetic aperture methods to increase the reconstructed bandwidth (*34*, *35*). It is common in the x-ray microscopy community to quote the half-period distance as spatial resolution, but this is not technically accurate. Here, we only refer to full-period distances and note that our achieved resolution of 8 nm is only the second reported full-period value below 10 nm, both having been achieved with x-ray energies below 2 keV (*10*).

We have described a new microscope for ultrahigh-resolution coherent soft x-ray imaging at the Advanced Light Source, which provides routine access to conventional STXM and advanced imaging modes such as ptychographic microscopy with complex sample environments. The combination of our high-brightness x-ray source, environmental control, ultrastable scanning system, advanced detectors, and fully integrated high-performance computing provides an easy-to-use platform for scientists to study materials with very high spatial resolution and chemical sensitivity. For the case of resonant imaging, our microscope routinely achieves sub–10-nm full-period spatial resolution and, while imaging off resonance, can improve the resolution and contrast over conventional STXM. Conventional STXM is integrated as a fast and robust method of sample precharacterization, while both imaging modes can readily make use

of commercial sample environments for studying electrochemical or catalytic reactions. As the brightness of synchrotron x-ray sources continues to rise, particularly with the development of diffraction-limited storage rings, these technologies will push x-ray microscopy toward wavelength-limited spatial resolution with ptychographic imaging and nanosecond time resolution with conventional imaging. These capabilities will revolutionize the study of chemical phases in active nanomaterials.

MATERIALS AND METHODS

Mechanical performance

The microscope uses a compact design that resides entirely within an 8-inch-diameter cylindrical vacuum chamber that provides optimum stability with regards to vibrations and thermal expansion, similar to the geometry used by TEM (fig. S3). The x-ray optical system, sample stage, and detectors are all mounted directly to a central cylindrical block that is aligned in its entirety to the x-ray beam. The optical system, described below, is modular in that it contains all degrees of freedom required for zone plate imaging; thus, it can readily be replaced or repurposed in other instruments. A central design decision was to place all coarse sample motions outside of vacuum and to limit their range and speed to maximize system stiffness and minimize thermal effects due to vacuum stepper motors. This is accomplished through the use of the CompuStage sample manipulator from Thermo Fisher Scientific (www.thermofisher.com). This stage has four degrees of sample motion (three translations and one rotation) with specifications for vibration and drift that are commensurate with the ultimate resolution goal for this x-ray microscope (angstrom-level vibration and drift rate of 1 nm/min). Besides a high degree of sample position stability, the primary impact of this design choice is that the sample must remain stationary while the x-ray focusing element (in this case, a zone plate) is scanned instead. The external coarse sample positions are used for global sample alignment, while all precision microscopy is accomplished with the integrated zone plate scanning mechanism with an imaging range of 100 μm by 100 μm.

The main imaging mechanism is a compact zone plate scanner that incorporates six motions [three for the zone plate and three for the order sorting aperture (OSA)] within a piezo flexure stage (fig. S4, right). The two axes of the piezo flexure stage correspond with the two image coordinates, and they carry the other four degrees of freedom along while scanning. The OSA stages and the zone plate focus stage are scanned along with the zone plate during imaging. The position of the zone plate relative to the cylinder axis is encoded by two interferometer beams, whose optics are mounted to the central block and which provide quadrature data to the piezo controller for closed-loop positioning. This positioning scheme relies on the inherent stability of the central cylindrical block and of the components mounted to it, i.e., sample stage and piezo flexure. Figure 5 (left) shows the spectrum of static position data measured at 20-kHz sampling frequency. In open loop, servo off, there is a peak at low frequency due to system drift; however, when the servo loop is turned on, the drift is compensated whereas the vibrations at higher frequency increase slightly to a root mean square value of 2.5 nm. The spectrum indicates a few sharp peaks at lower frequency in the vicinity of 60 Hz due to environmental excitation and a broad peak at 320 Hz, which is the natural resonant frequency of the scanning stage relative to the central block. Although the interferometer can sample the stage positions at up to 2 MHz and the piezo controller feedback loop updates at 1 kHz, the bandwidth of the entire control system, which limits the maximum achievable scanning speed, is dominated by the mechanical characteristics of the stages under closed-loop control. The bandwidth of the control system, including stage mechanics, can be measured directly by comparing the achieved oscillation amplitude to the commanded amplitude as a function of oscillation frequency. The system bandwidth is the frequency at which the achieved amplitude has dropped by 1 dB (about 30%). Figure 5 (right) shows a comparison between the current design and a conventional system, which includes in-vacuum stepper motors that carry the piezo scanner (*36*). These conventional systems are inherently less stable because of the massive stages and only achieve a bandwidth of 22 Hz, whereas our design has more than three times the bandwidth at 70 Hz. This higher bandwidth results in fast step scanning, as shown in the inset where a typical scan step is achieved in about 8 ms, which is comparable to the total system overhead per scan point and is 10 times smaller than the x-ray exposure time for very high resolution ptychographic imaging. For this reason, it is not advantageous to do fly scanning ptychography, which increases the computational overhead. On the other hand, conventional STXM is routinely executed in fly-scan mode and with 70-Hz bandwidth, and a 1-μm^2 area can be imaged at 14 frames per second with a 50-μs x-ray exposure per 50-nm pixel. The planned diffraction-limited storage ring upgrade at the Advanced Light Source will provide this x-ray flux from each 100-ps-long electron bunch.

The x-ray focusing element is a 360-μm-diameter Fresnel zone plate with 45-nm outer zone width and 300-nm-thick Au zones that provide an optimum efficiency of 18% at 1500-eV x-ray energy. This optic has a Rayleigh resolution of about 55 nm, which is still quite useful for conventional microscopy, and requires a 40-nm step for ptychographic imaging while operating in focus. The ptychographic step size can be larger than one-half of the Rayleigh resolution because of the strong contribution from the tails of the focus, which is enhanced by the use of a central stop with a diameter of 95 μm. The focal length is also long enough across the spectral range to allow use of complex environments and sample rotation.

Microscope infrastructure

The x-ray microscope is situated at beamline 7.0.1.2 [Coherent Scattering and Microscopy (COSMIC)] of the Advanced Light Source, which uses an elliptically polarizing undulator x-ray source that provides full x-ray polarization control from 250 eV to 2.5 keV. The beamline design is described in detail elsewhere; however, we review it briefly for clarity (*37*). The optical system makes use of a collimated plane grating monochromator, which provides an energy-resolving power ($E/\Delta E$) of about 2500, and rhodium-coated optics for high efficiency at the high end of the energy spectrum. Overall, the beamline efficiency is such that it provides 3×10^{10} coherent photons per second to the imaging zone plate at 1 keV and about one order of magnitude lower flux at 2.5-keV x-ray energy.

An environmental enclosure serves to isolate the microscope from temperature drift and ambient mechanical excitation. Closed-loop temperature control maintains the air and equipment with below 0.1°C variation over 24 hours (fig. S5). A massive support structure was designed to both isolate the microscope from floor vibrations and prevent deflections of the secondary source aperture (exit slit) with respect to the microscope due to elastic deformation of the concrete floor under transient load, which could induce distortions

and intensity changes. A base frame made of steel tube filled with polymer composite, for high thermal stability, supports all equipment (fig. S4). The elevated portion of the frame extends outside of the environmental enclosure. The exit slit is elevated off the concrete floor since it is in proximity to work areas, which may induce elastic deformation of the floor, thereby shifting slightly the source position. Inside the enclosure, a large composite table is suspended within the steel frame, resting on several polymer foam pads, which passively damp vibrations with frequencies above 13 Hz. Although the area surrounding the microscope enclosure is exposed to groups of people and moving equipment, the microscope itself sees little disturbance (fig. S6).

Data acquisition and analysis

The microscope uses two independent detectors for the two basic modes of operation: STXM and ptychography. A silicon photodiode with active area of 2 mm by 5 mm is used for total transmission measurements during conventional imaging, while a high–frame rate CCD detector (fastCCD) is used for ptychographic measurements (*38*). Figure S7 shows a schematic of the system controls and data acquisition pipeline. A PC (STXM control computer) communicates with a timer/counter card via the PCI Express (peripheral component interconnect) bus and the piezo controller via USB. The timer card synchronizes the triggering of the x-ray shutter and both detectors with microsecond accuracy while also counting pulsed data from the diode. The diode detector chain uses a current amplifier (typical gain, 10^8 V/A) and subsequent voltage-to-frequency converter operating at 25 MHz to generate pulses with a digitized photon flux resolution of 50 photons per count at 1000 eV. With a total flux of 1×10^9 photons per second, typical dwell times for STXM imaging are 50 μs, which yield 1000 detector counts and typically about 10 noise counts per pixel, giving a total signal-to-noise ratio of 24, including photon noise. Highly absorbing samples or those that require low flux can use higher gain on the amplifier and frequency converter to improve the flux resolution by a factor of 10. Alternatively, a single photon-counting avalanche photodiode could be used at higher energies.

For ptychographic measurements, the diode detector is automatically translated to the side, thus exposing the fastCCD sensor while both detectors are triggered by the same timing pulse. The detector frame rate is limited by the x-ray exposure time to about 40 frames per second but is capable of 100 frames per second. For each diffraction frame, the fastCCD generates a stream of user datagram protocol packets, which are assembled on a local server into complete diffraction patterns (960 × 960 pixels) before being saved into TIFF files on a remote cluster with a data transfer node (DTN) over a dedicated 10-Gbps network. The metadata that relates all TIFF files as a scan is saved separately by the STXM control PC onto the same DTN via a separate 1-Gbps control network. Three data acquisition modes are possible: single frame at each point, multiple identical frames at each point, or a single short and a single long exposure at each point (called double-exposure mode, typically 5 and 50 ms). The third option is the most common, as it achieves high resolution with few datasets that are assembled into single diffraction patterns during postprocessing in a manner similar to high dynamic range photography. Once the first few TIFF files are saved, the computational steps begin with a preprocessor that is CPU-bound code running on a node with 44 CPU cores, the preprocessor node. The preprocessor subtracts the fastCCD dark frame, measured at the start of each scan, crops or pads the data to the requested spatial frequency range around the optical axis, and reduces the sampling to typically 256 × 256 pixels for faster reconstruction when working with the microscope in focus (*39*). This computational step proceeds in batches during the scan and readily keeps pace with the data acquisition. Optionally, the preprocessor can save each processed batch in the open-ended .ptyd format (HDF5) of PtyPy (*40*) and transfer it to any computation end point in the wider Science DMZ network of ESnet (*41*). For the more common case of local reconstruction, once all TIFF files are processed, the results are saved into a single HDF5 file formatted according to the Coherent X-ray Imaging Data Bank standard and submitted for reconstruction using the SHARP GPU (graphics processing unit) code (*42*, *43*). Typical reconstructions span eight GPUs (NVIDIA Titan RTX) and use the following configuration: 500 iterations of either relaxed averaged alternating reflections (RAAR) or alternating direction method of multipliers algorithms, probe and background refinement every other iteration, and a beta value of 0.5 when using RAAR (*12*). Reconstruction time is about 5 s/μm^2, which compares well with the data acquisition time of about 60 s/μm^2 in double-exposure mode. Reconstructed image pixels are routinely 5 nm in size; thus, we record over 600 pixels per second including high-resolution data acquisition and reconstruction.

SUPPLEMENTARY MATERIALS

Supplementary material for this article is available at http://advances.sciencemag.org/cgi/content/full/6/51/eabc4904/DC1

REFERENCES AND NOTES

1. J. Kirz, C. Jacobsen, M. Howells, Soft x-ray microscopes and their biological applications. *Q. Rev. Biophys.* **28**, 33–130 (1995).
2. C. Holzner, M. Feser, S. Vogt, B. Hornberger, S. B. Baines, C. Jacobsen, Zernike phase contrast in scanning microscopy with x-rays. *Nat. Phys.* **6**, 883–887 (2010).
3. R. Falcone, C. Jacobsen, J. Kirz, S. Marchesini, D. Shapiro, J. Spence, New directions in x-ray microscopy. *Contemp. Phys.* **52**, 293–318 (2011).
4. F. Pfeiffer, X-ray ptychography. *Nat. Photonics* **12**, 9–17 (2018).
5. W. Chao, P. Fischer, T. Tyliszczak, S. Rekawa, E. Anderson, P. Naulleau, Real space soft x-ray imaging at 10 nm spatial resolution. *Opt. Express* **20**, 9777–9783 (2012).
6. S. Rehbein, S. Heim, P. Guttmann, S. Werner, G. Schneider, Ultrahigh-resolution soft-x-ray microscopy with zone plates in high orders of diffraction. *Phys. Rev. Lett.* **103**, 110801 (2009).
7. H. Yan, N. Bouet, J. Zhou, X. Huang, E. Nazaretski, W. Xu, A. P. Cocco, W. K. S. Chiu, K. S. Brinkman, Y. S. Chu, Multimodal hard x-ray imaging with resolution approaching 10 nm for studies in material science. *Nano Futures* **2**, 011001 (2018).
8. M. Guizar-Sicairos, I. Johnson, A. Diaz, M. Holler, P. Karvinen, H.-C. Stadler, R. Dinapoli, O. Bunk, A. Menzel, High-throughput ptychography using Eiger: Scanning x-ray nano-imaging of extended regions. *Opt. Express* **22**, 14859–14870 (2014).
9. A. Schropp, R. Hoppe, J. Patommel, D. Samberg, F. Seiboth, S. Stephan, G. Wellenreuther, G. Falkenberg, C. G. Schroer, Hard x-ray scanning microscopy with coherent radiation: Beyond the resolution of conventional x-ray microscopes. *Appl. Phys. Lett.* **100**, 253112–253113 (2012).
10. D. A. Shapiro, Y.-S. Yu, T. Tyliszczak, J. Cabana, R. Celestre, W. Chao, K. Kaznatcheev, A. L. D. Kilcoyne, F. Maia, S. Marchesini, Y. Shirley Meng, T. Warwick, L. L. Yang, H. A. Padmore, Chemical composition mapping with nanometre resolution by soft x-ray microscopy. *Nat. Photonics* **8**, 765–769 (2014).
11. J. Deng, D. J. Vine, S. Chen, Y. S. G. Nashed, Q. Jin, N. W. Phillips, T. Peterka, R. Ross, S. Vogt, C. J. Jacobsen, Simultaneous cryo x-ray ptychographic and fluorescence microscopy of green algae. *Proc. Natl. Acad. Sci.* **112**, 2314–2319 (2015).
12. S. Marchesini, A. Schirotzek, C. Yang, H.-t. Wu, F. Maia, Augmented projections for ptychographic imaging. *Inverse Probl.* **29**, 115009 (2013).
13. D. F. Gardner, M. Tanksalvala, E. R. Shanblatt, X. Zhang, B. R. Galloway, C. L. Porter, R. Karl Jr., C. Bevis, D. E. Adams, H. C. Kapteyn, M. M. Murnane, G. F. Mancini, Subwavelength coherent imaging of periodic samples using a 13.5 nm tabletop high-harmonic light source. *Nat. Photonics* **11**, 259–263 (2017).
14. C. Steier, A. Anders, J. M. Byrd, K. Chow, S. De Santis, R. M. Duarte, J.-Y. Jung, T. H. Luo, H. Nishimura, T. Oliver, J. R. Osborn, H. A. Padmore, G. C. Pappas, S. Persichelli, D. Robin, F. Sannibale, D. Schlueter, C. Sun, C. A. Swenson, M. Venturini, W. L. Waldron, E. J. Wallén,

W. Wan, Y. C. Yang, *ALS-U: A Soft X-Ray Diffraction Limited Light Source* (JACoW, 2017), pp. 263–265.
15. K. W. Bossers, R. Valadian, S. Zanoni, R. Smeets, N. Friederichs, J. Garrevoet, F. Meirer, B. M. Weckhuysen, Correlated x-ray ptychography and fluorescence nano-tomography on the fragmentation behavior of an individual catalyst particle during the early stages of olefin polymerization. *J. Am. Chem. Soc.* **142**, 3691–3695 (2020).
16. Y.-S. Yu, M. Farmand, C. Kim, Y. Liu, C. P. Grey, F. C. Strobridge, T. Tyliszczak, R. Celestre, P. Denes, J. Joseph, H. Krishnan, F. R. N. C. Maia, A. L. D. Kilcoyne, S. Marchesini, T. P. C. Leite, T. Warwick, H. Padmore, J. Cabana, D. A. Shapiro, Three-dimensional localization of nanoscale battery reactions using soft x-ray tomography. *Nat. Commun.* **9**, 921 (2018).
17. C. Donnelly, V. Scagnoli, M. Guizar-Sicairos, M. Holler, F. Wilhelm, F. Guillou, A. Rogalev, C. Detlefs, A. Menzel, J. Raabe, L. J. Heyderman, High-resolution hard x-ray magnetic imaging with dichroic ptychography. *Phys. Rev. B* **94**, 064421 (2016).
18. M. Holler, J. Raabe, A. Diaz, M. Guizar-Sicairos, R. Wepf, M. Odstrcil, F. R. Shaik, V. Panneels, A. Menzel, B. Sarafimov, S. Maag, X. Wang, V. Thominet, H. Walther, T. Lachat, M. Vitins, O. Bunk, OMNY—A tOMography Nano crYo stage. *Rev. Sci. Instrum.* **89**, 043706 (2018).
19. J. Deng, C. Preissner, J. A. Klug, S. Mashrafi, C. Roehrig, Y. Jiang, Y. Yao, M. Wojcik, M. D. Wyman, D. Vine, K. Yue, S. Chen, T. Mooney, M. Wang, Z. Feng, D. Jin, Z. Cai, B. Lai, S. Vogt, The Velociprobe: An ultrafast hard x-ray nanoprobe for high-resolution ptychographic imaging. *Rev. Sci. Instrum.* **90**, 083701 (2019).
20. V. V. Yashchuk, P. J. Fischer, E. R. Chan, R. Conley, W. R. McKinney, N. A. Artemiev, N. Bouet, S. Cabrini, G. Calafiore, I. Lacey, C. Peroz, S. Babin, Binary pseudo-random patterned structures for modulation transfer function calibration and resolution characterization of a full-field transmission soft x-ray microscope. *Rev. Sci. Instrum.* **86**, 123702 (2015).
21. S. Babin, G. Calafiore, C. Peroz, R. Conley, N. Bouet, S. Cabrini, E. Chan, I. Lacey, W. R. Mc Kinney, V. V. Yashchuk, A. E. Vladar, 1.5 nm fabrication of test patterns for characterization of metrological systems. *J. Vac. Sci. Technol.* **33**, 06FL01 (2015).
22. M. Farmand, R. Celestre, P. Denes, A. L. D. Kilcoyne, S. Marchesini, H. Padmore, T. Tyliszczak, T. Warwick, X. Shi, J. Lee, Y.-S. Yu, J. Cabana, J. Joseph, H. Krishnan, T. Perciano, F. R. N. C. Maia, D. A. Shapiro, Near-edge x-ray refraction fine structure microscopy. *Appl. Phys. Lett.* **110**, 063101 (2017).
23. P. Guttmann, C. Bittencourt, S. Rehbein, P. Umek, X. Ke, G. Van Tendeloo, C. P. Ewels, G. Schneider, Nanoscale spectroscopy with polarized x-rays by NEXAFS-TXM. *Nat. Photonics* **6**, 25–29 (2012).
24. H. Ade, A. P. Hitchcock, NEXAFS microscopy and resonant scattering: Composition and orientation probed in real and reciprocal space. *Polymer* **49**, 643–675 (2008).
25. Y.-S. Yu, C. Kim, D. A. Shapiro, M. Farmand, D. Qian, T. Tyliszczak, A. L. D. Kilcoyne, R. Celestre, S. Marchesini, J. Joseph, P. Denes, T. Warwick, F. C. Strobridge, C. P. Grey, H. Padmore, Y. S. Meng, R. Kostecki, J. Cabana, Dependence on crystal size of the nanoscale chemical phase distribution and fracture in LixFePO4. *Nano Lett.* **15**, 4282–4288 (2015).
26. U. Boesenberg, F. Meirer, Y. Liu, A. K. Shukla, R. D. Anna, T. Tyliszczak, G. Chen, J. C. Andrews, T. J. Richardson, R. Kostecki, J. Cabana, Mesoscale phase distribution in single particles of $LiFePO_4$ following lithium deintercalation. *Chem. Mater.* **25**, 1664–1672 (2013).
27. G. Chen, X. Song, T. J. Richardson, Metastable solid-solution phases in the $LiFePO_4$ $FePO_4$ system. *J. Electrochem. Soc.* **154**, A627 (2007).
28. C. A. Larabell, M. A. Le Gros, X-ray tomography generates 3-D reconstructions of the yeast, *Saccharomyces cerevisiae*, at 60-nm resolution. *Mol. Biol. Cell* **15**, 957–962 (2004).
29. E. Hummel, P. Guttmann, S. Werner, B. Tarek, G. Schneider, M. Kunz, A. S. Frangakis, B. Westermann, 3D ultrastructural organization of whole Chlamydomonas reinhardtii cells studied by nanoscale soft x-ray tomography. *PLOS ONE* **7**, e53293 (2012).
30. S. H. Shahmoradian, E. H. R. Tsai, A. Diaz, M. Guizar-Sicairos, J. Raabe, L. Spycher, M. Britschgi, A. Ruf, H. Stahlberg, M. Holler, Three-dimensional imaging of biological tissue by cryo x-ray ptychography. *Sci. Rep.* **7**, 6291 (2017).
31. A. Sorrentino, J. N. Ås, R. V. Ärcel, F. J. C. Ãn, M. Rosanes, J. Avila, A. Tkachuk, J. Irwin, S. Ferrer, E. Pereiro, MISTRAL: A transmission soft x-ray microscopy beamline for cryo nano-tomography of biological samples and magnetic domains imaging. *J. Synchrotron Radiat.* **22**, 1112–1117 (2015).
32. J. Deng, Y. H. Lo, M. Gallagher-Jones, S. Chen, A. Pryor Jr., Q. Jin, Y. P. Hong, Y. S. G. Nashed, S. Vogt, J. Miao, C. Jacobsen, Correlative 3D x-ray fluorescence and ptychographic tomography of frozen-hydrated green algae. *Sci. Adv.* **4**, eaau4548 (2018).
33. Julio C. da Silva, A. Pacureanu, Y. Yang, F. Fus, M. Hubert, L. Bloch, M. Salome, S. Bohic, P. Cloetens, High-energy cryo x-ray nano-imaging at the ID16A beamline of ESRF, in *X-Ray Nanoimaging: Instruments and Methods III* (International Society for Optics and Photonics, 2017), vol. 10389, p. 103890F.
34. A. M. Maiden, M. J. Humphry, F. Zhang, J. M. Rodenburg, Superresolution imaging via ptychography. *J. Opt. Soc. Am. A* **28**, 604–612 (2011).
35. D. Claus, J. M. Rodenburg, Diffraction-limited superresolution ptychography in the Rayleigh–Sommerfeld regime. *JOSA A* **36**, A12–A19 (2019).
36. A. L. D. Kilcoyne, T. Tyliszczak, W. F. Steele, S. Fakra, P. Hitchcock, K. Franck, E. Anderson, B. Harteneck, E. G. Rightor, G. E. Mitchell, A. P. Hitchcock, L. Yang, T. Warwick, H. Ade, Interferometer-controlled scanning transmission x-ray microscopes at the Advanced Light Source. *J. Synchrotron Radiat.* **10**, 125–136 (2003).
37. D. Shapiro, S. Roy, R. Celestre, W. Chao, D. Doering, M. Howells, S. Kevan, D. Kilcoyne, J. Kirz, S. Marchesini, K. A. Seu, A. Schirotzek, J. Spence, T. Tyliszczak, T. Warwick, D. Voronov, H. A. Padmore, Development of coherent scattering and diffractive imaging and the COSMIC facility at the Advanced Light Source. *J. Phys. Conf. Ser.* **425**, 192011 (2013).
38. P. Denes, D. Doering, H. A. Padmore, J.-P. Walder, J. Weizeorick, A fast, direct x-ray detection charge-coupled device. *Rev. Sci. Instrum.* **80**, 083302 (2009).
39. B. Enders, K. Nowrouzi, H. Krishnan, S. Marchesini, J. Park, Y.-S. Yu, D. A. Shapiro, Dataflow at the COSMIC beamline—Stream processing and supercomputing. *Microsc. Microanal.* **24**, 56–57 (2018).
40. B. Enders, P. Thibault, A computational framework for ptychographic reconstructions. *Proc. R. Soc. A* **472**, 20160640 (2016).
41. J. Crichigno, E. Bou-Harb, N. Ghani, A comprehensive tutorial on science DMZ. *IEEE Commun. Surveys Tutorials* **21**, 2041–2078 (2019).
42. S. Marchesini, H. Krishnan, B. J. Daurer, D. A. Shapiro, T. Perciano, J. A. Sethian, F. R. N. C. Maia, SHARP: A distributed GPU-based ptychographic solver. *J. Appl. Cryst.* **49**, 1245–1252 (2016).
43. F. R. N. C. Maia, The coherent x-ray imaging data bank. *Nat. Methods* **9**, 854–855 (2012).

Acknowledgments

Funding: This research used resources of the Advanced Light Source, a DOE Office of Science User Facility under contract no. DE-AC02-05CH11231. This work was partially supported by STROBE, an NSF Science and Technology Center, under grant no. DMR 1548924, by the U.S. Department of Energy Office of Science, Office of Basic Energy Sciences, and Small Business Technology Transfer programs under award number DE-SC0011352 and the National Synchrotron Light Source II and Advanced Photon Source under contract nos. DE-SC0012704 and DE-AC02-06CH11357, respectively. **Author contributions:** D.A.S., H.P., and T.W. directed the project. R.S.C., K.N., and D.A.S. designed and built the microscope. B.E., H.K., S.M., P.E., and L.Y. designed software for data acquisition and analysis. W.C. and S.R.O. fabricated x-ray optics. S.J. and K.M. implemented high-performance computing for data analysis. S.B., R.P.C., and V.V.Y. implemented samples and methods for resolution analysis. P.D. and J.M.J. implemented a fast x-ray detector. Y.-S.Y., K.N., J.Z., and D.A.S. collected and analyzed the data. D.S. wrote the manuscript with input from all the authors. **Competing interests:** The authors declare that they have no competing interests. **Data and materials availability:** All data needed to evaluate the conclusions in the paper are present in the paper and/or the Supplementary Materials. All ptychography data are available for download at www.cxidb.org (ID 162). Additional data related to this paper may be requested from the authors.

Submitted 27 April 2020
Accepted 2 November 2020
Published 16 December 2020
10.1126/sciadv.abc4904

Citation: D. A. Shapiro, S. Babin, R. S. Celestre, W. Chao, R. P. Conley, P. Denes, B. Enders, P. Enfedaque, S. James, J. M. Joseph, H. Krishnan, S. Marchesini, K. Muriki, K. Nowrouzi, S. R. Oh, H. Padmore, T. Warwick, L. Yang, V. V. Yashchuk, Y.-S. Yu, J. Zhao, An ultrahigh-resolution soft x-ray microscope for quantitative analysis of chemically heterogeneous nanomaterials. *Sci. Adv.* **6**, eabc4904 (2020).